2024 IEEE/RSJ International Conference on Intelligent Robots and Systems (IROS)
October 14-18, 2024. Abu Dhabi, UAE

X-Ray-Guided Magnetic Fields for Wireless Control of Untethered Magnetic Robots in Cerebral Vascular Phantoms

Leendert-Jan W. Ligtenberg[1,2,3], Marcus C. J. de Boer[1,2], Iris Mulder[1,2], Roger Lomme[3]
Dorothee Wasserberg[4,5] Emily A. M. Klein Rot[4], Doron Ben Ami[6], Udi Sadeh[6], H. Remco Liefers[2]
Oded Shoseyov[6,7], Pascal Jonkheijm[4,5], Michiel Warlé[3], and Islam S. M. Khalil[1,2]

***Abstract*— This paper explores the application of X-ray-guided magnetic fields for the wireless control of untethered magnetic robots (UMRs) within cerebral vascular phantoms. With a focus on addressing challenges associated with strokes and brain aneurysms, the study aims to enhance neurosurgical procedures by improving precision and maneuverability. Experimental findings showcase the feasibility and effectiveness of this innovative approach in navigating UMRs, characterized by a screw-shaped body and a ferromagnetic core, through complex vascular structures. Cone-beam computed tomography is employed to determine the tomography and provide various reference trajectories for the UMR inside the cerebral vascular phantom. Our motion control experiments show that the X-ray-guided magnetic fields enable the UMR to move along any intended path with an average success rate of 89%, allowing the UMR to move between the left and right common carotid artery to the left and right internal and external carotid artery.**

I. INTRODUCTION

In the realm of neurosurgery, strokes and brain aneurysms present significant challenges due to the intricate nature of the cerebral vasculature. Traditional surgical approaches may involve invasive procedures with inherent risks and the success of current catheter and guidewire-based methods in peripheral intervention is limited by the competing requirements and tradeoffs between stiffness, diameter, and controllability. Therefore, there is a growing interest in developing innovative techniques that enhance precision and minimize patient trauma [1]-[5]. One promising avenue is the use of untethered magnetic robots (UMRs) guided by X-ray Fluoroscopy imaging, which holds potential for revolutionizing neurosurgical interventions. This paper explores the application of wireless control of UMRs within cerebral vascular phantoms, leveraging X-ray-guided magnetic fields to navigate through complex vascular structures with enhanced accuracy and safety.

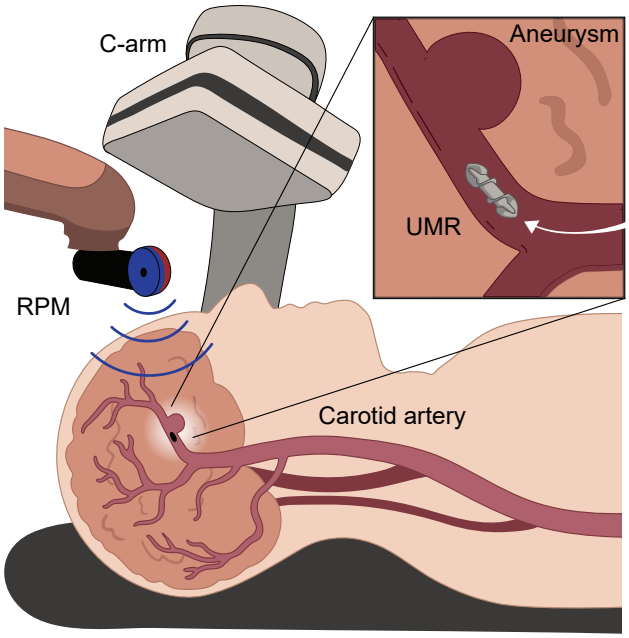

Fig. 1. Untethered magnetic robots (UMRs) offer a novel approach for navigating bodily fluids, enabling access to hard-to-reach regions within the human body. This technology presents an alternative minimally invasive solution for addressing strokes and brain aneurysms, enhancing the precision and safety of neurosurgical interventions. UMRs can be controllably moved toward the desired target using X-ray-guided magnetic fields. A robotic C-arm is utilized for precise localization and mapping of the vascular network's tomography, while a rotating magnetic field enables wireless actuation along any desired vascular route.

Strokes and brain aneurysms are among the most critical neurological conditions, often resulting in severe disabilities or fatalities. Strokes occur when blood flow to the brain is disrupted, leading to tissue damage, while brain aneurysms involve the weakening and ballooning of blood vessel walls, posing a risk of rupture and hemorrhage (Fig. 1). Both conditions necessitate precise and minimally invasive treatment strategies to mitigate their devastating effects and improve patient outcomes. Wang *et al*. have proposed a wireless stent-shaped magnetic soft robot for navigating and performing medical interventions in distal vascular regions, facilitating new minimally invasive endovascular procedures [6]. Simi-

[1]The authors are with RAM—Robotics and Mechatronics, University of Twente, 7500 AE Enschede, The Netherlands.
[2]The authors are with the Technical Medical Centre, University of Twente, 7500 AE Enschede, The Netherlands.
[3]The authors are with Radboud University Medical Center, 6525 GA Nijmegen, The Netherlands.
[4]LipoCoat B.V., 7521 AG Enschede, The Netherlands.
[5]Laboratory of Biointerface Chemistry, Technical Medical Centre, University of Twente, 7500 AE Enschede, The Netherlands.
[6]The authors are with Triticum Medical, 4726389 Ramat HaSharon, Israel.
[7]O. Shoseyov is with The Hebrew University of Jerusalem, 76100 Rehovot, Israel.

The collaboration project is co-funded by the PPP Allowance made available by Health∼Holland, Top Sector Life Sciences & Health, to the University of Twente to stimulate public-private partnerships. This project has been supported by the Pioneers in Healthcare Innovation funding.

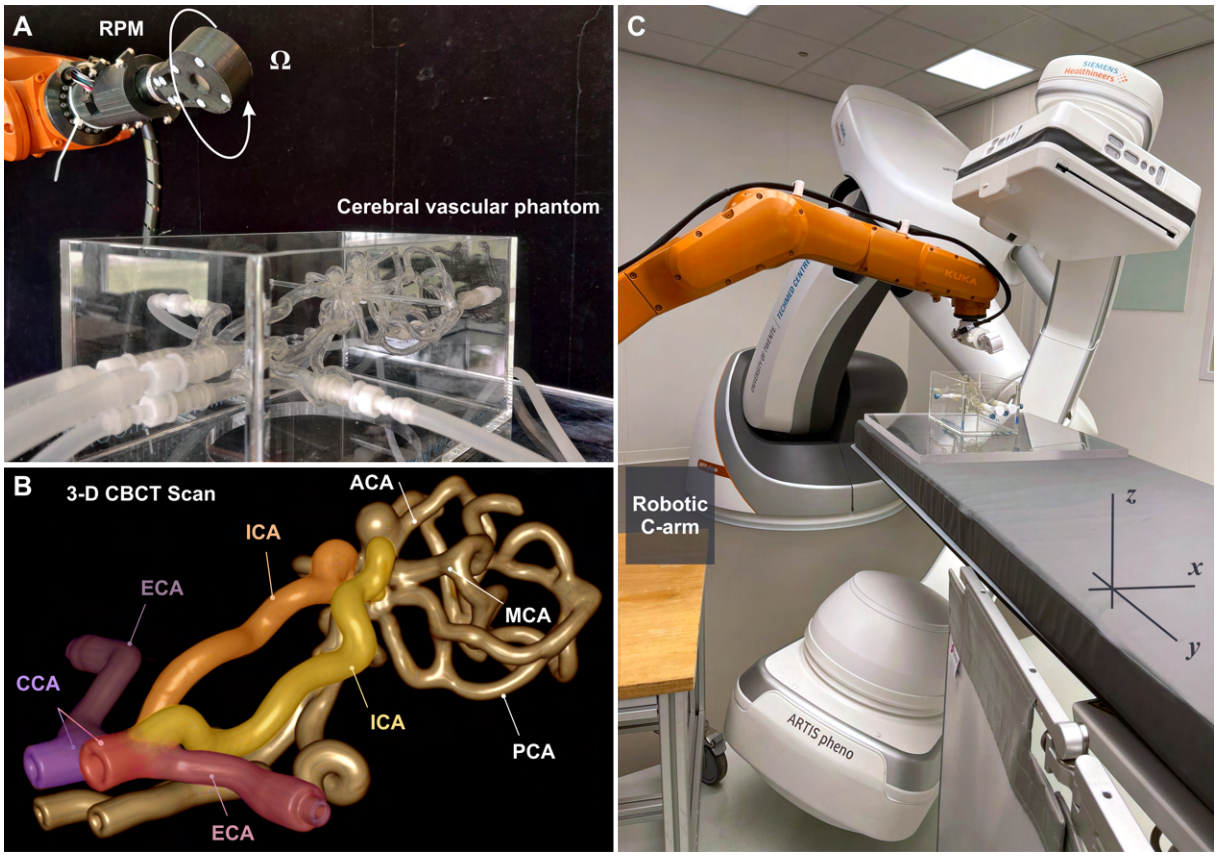

Fig. 2. Navigating within a cerebral vascular phantom, untethered magnetic robots (UMRs) measuring 9 mm in length and 3 mm in diameter are controlled using X-ray-guided magnetic fields. Demonstrating agility, (A) the rotation axis of the magnetic field aligns parallel with the centerline of the vessel. (B) The vascular model is reconstructed using cone-beam computed tomography (CBCT) scans. A 4-mm-diameter UMR can navigate from the common carotid artery (CCA) toward the external carotid artery (ECA) and the internal carotid artery (ICA). The UMR is unable to access the posterior cerebral artery (PCA), anterior cerebral artery (ACA), and middle cerebral artery (MCA) due to its size limitation. (C) X-ray Fluoroscopy images and CBCT scans are obtained using a robotic C-arm for wireless control and to determine the tomography of the environment, respectively.

larly, Yang *et al*. have introduced a UMR capable of high-speed upstream movement in blood vessels and performing various biomedical tasks, such as drug delivery and tissue biopsy [7]. The robot's streamlined design and bioinspired features enable controllable, minimally invasive endovascular interventions, advancing the development of wireless millirobots for biomedical applications. Jin *et al*. have introduced a catheterization-integrated swarming microrobotic platform for targeted embolization treatment of aneurysms. It utilizes *p*H-responsive self-healing hydrogel microgels, guided by ultrasound and fluoroscopy imaging, and triggered by an external magnetic field for effective embolization [8].

UMRs controlled by X-ray-guided magnetic fields represent a cutting-edge technology in the field of minimally invasive surgery, offering the potential for precise and targeted interventions within delicate anatomical structures [9]. These robots can navigate through the body using external magnetic fields (Fig. 1), enabling minimally invasive procedures with reduced tissue damage and shorter recovery times [10], [11]. The integration of X-ray guidance further enhances navigation accuracy and real-time visualization of UMRs, facilitating intricate maneuvers in challenging anatomical regions such as the cerebral vasculature. This approach holds promise for improving the treatment of strokes and brain aneurysms, two critical neurological conditions with significant morbidity and mortality rates. By combining UMRs with X-ray imaging, neurosurgeons can achieve unprecedented levels of precision and safety in their interventions, ultimately leading to better patient outcomes and enhanced quality of care.

The remainder of this paper is organized as follows: Section II provides descriptions pertaining to the UMRs, the robotic C-arm, the wireless manipulation system, and the vascular model. Section III presents the frequency response experimental results of the confined UMR and provides experimental results of the UMR inside the cerebral vascular phantom. Finally, Section IV concludes the paper and provides directions for our future work.

II. X-RAY-GUIDED UNTETHERED MAGNETIC ROBOTS

When a magnetically actuated screw-shaped body is contained within a three-dimensional (3D) confinement and is subjected to a rotating magnetic field with a rotation axis parallel to the centerline of the confinement, it will move forward or backward based on the direction of the field.

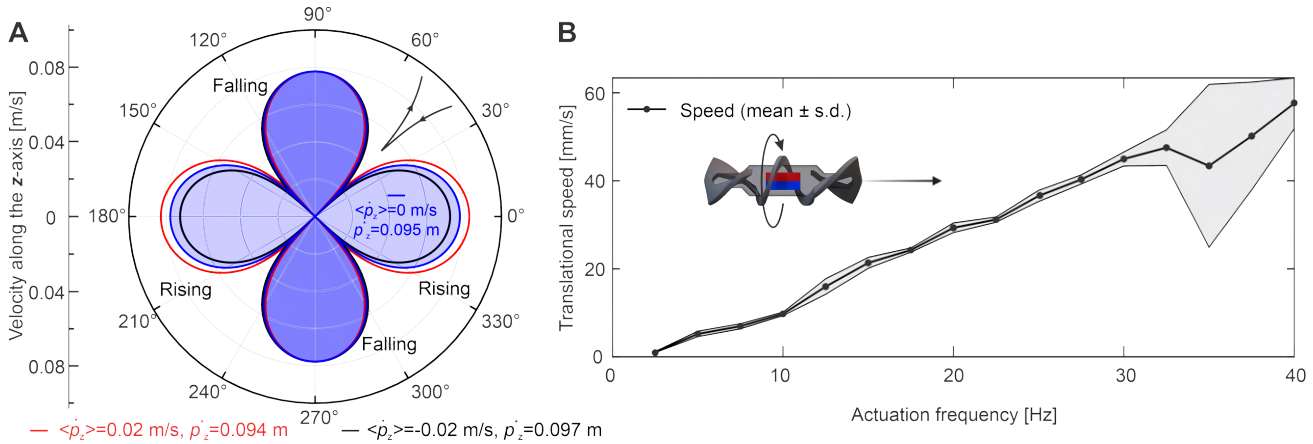

Fig. 3. Characterization of the active suspension of the untethered magnetic robot (UMR) and frequency response. (A) Active suspension is achieved by synchronously rotating the UMR and the RPM actuator, with the RPM-UMR gap controlled at 0.095 m. The vertical velocity component, represented by rose curves, is calculated using Equation 1 for $m = 6.2 \times 10^{-4}$ A.m^2, $M = 19.9$ A.m^2, and $\rho = 997$ kg/m^3. The angle bracket denotes averaging over one rotation period. (B) Translational speeds at varying actuation frequencies up to the maximum frequency are depicted. The *in vitro* experiment was conducted in water with a stationary RPM positioned 15 cm from the tube, which had a diameter of 9.525 mm. A linear relationship between the frequency and translational speed is evident.

The rotation axis of the magnetic field can be controlled by robotically controlling the pose of a rotating permanent magnet (RPM) [12], as shown in Fig. 2(A). Translating the RPM with respect to the UMR enables it to rotate in sync along an intended path inside a vascular system (Fig. 2(B)). Additionally, the RPM-UMR gap can be controlled simultaneously such that the weight of the UMR is compensated by the field-gradient pulling under X-ray guidance (Fig. 2(C)).

A. Design and Fabrication of Untethered Magnetic Robots

The UMRs are manufactured using additive techniques, allowing for the precise construction of screw-shaped bodies. Additionally, they are coated with a biocompatible material to enhance their compatibility within biological systems [9]. These bodies are designed to accommodate small permanent magnets, placed to provide the necessary propulsion and maneuverability within the vascular routes. This fabrication approach ensures the creation of UMRs with consistent dimensions and magnetic properties. When submerged in a viscous fluid with density ρ, the UMR's vertical displacement with respect to the RPM actuator, p_z, is governed by $\frac{1}{2}\rho \dot{p}_z^2 c_\mathrm{d} A = -F_\mathrm{m} - F_\mathrm{g}$. The left-hand side represents a drag component, arising from the resistance to translating the UMR along the z-axis. This resistance is balanced by the field gradient pulling, F_m, and the gravitational force, F_g, and yields

$$\dot{p}_z^2 = \frac{2}{\rho c_\mathrm{d} A}\left(\frac{1}{2}\frac{3\mu_0 M m}{2\pi p_z^4} - \Delta\rho g V\right), \qquad (1)$$

where c_d and A represent the lateral drag coefficient of the UMR and the cross-sectional area, respectively. Additionally, μ_0 denotes the permeability of free-space, while M and m denote the magnetic moment of the RPM actuator and the UMR, respectively. Further, $\Delta\rho$ is the density difference for the UMR and the surrounding fluid, g is the gravitational constant, and V the volume of the UMR.

Equation (1) is valuable for determining an optimal RPM-UMR gap that achieves a balance between magnetic and gravitational forces. If the RPM-UMR gap decreases below this optimal value, the field-gradient pulling will attract the UMR toward the RPM actuator. Conversely, if the RPM-UMR gap increases beyond this optimal value, the UMR will fall under the influence of its own weight. Fig. 3(A) displays three vertical velocity profiles (rose curves) for three RPM-UMR gaps. The solution of Equation (1) yields smooth curves arranged symmetrically about a common center, indicating that the velocity periodically increases to a maximum and then decreases to zero. However, there exists an optimal RPM-UMR gap (i.e., $p_z = 0.095$ m for a UMR and RPM of magnetic moment of $m = 6.2 \times 10^{-4}$ and $M = 19.9$ A.m^2, respectively) that yields zero vertical velocity on average. For an RPM-UMR gap of $p_z < 0.095$ m, the average vertical velocity component is greater than zero, indicating that the UMR would be attracted toward the RPM. In contrast, when the RPM-UMR gap is $p_z > 0.095$ m, the average vertical velocity component is less than zero, indicating that the UMR would move away from the RPM.

B. X-Ray-Guided Magnetic Control System

The tomography of the cerebral vascular phantom (Anatomical Vascular Model, HN-S-A-010, ELASTRAT, Switzerland) is generated from cone-beam computed tomography (CBCT) scans, as depicted in Fig. 2(B), using a robotic C-arm (Siemens Healthineers ArtisPheno, Erlangen, Germany). Using this tomography, each vascular route is mapped to determine the desired rotation axis for the magnetic field. This axis is adjusted according to the UMR's position along each vascular route (e.g., from the right common carotid artery to the right external carotid artery). Subsequently, the rotation axis of the RPM is controlled using the 6-degree-of-freedom manipulator (KUKA KR-10 1100-2, KUKA, Augsburg, Germany) shown in Fig. 2(C), while simultaneously

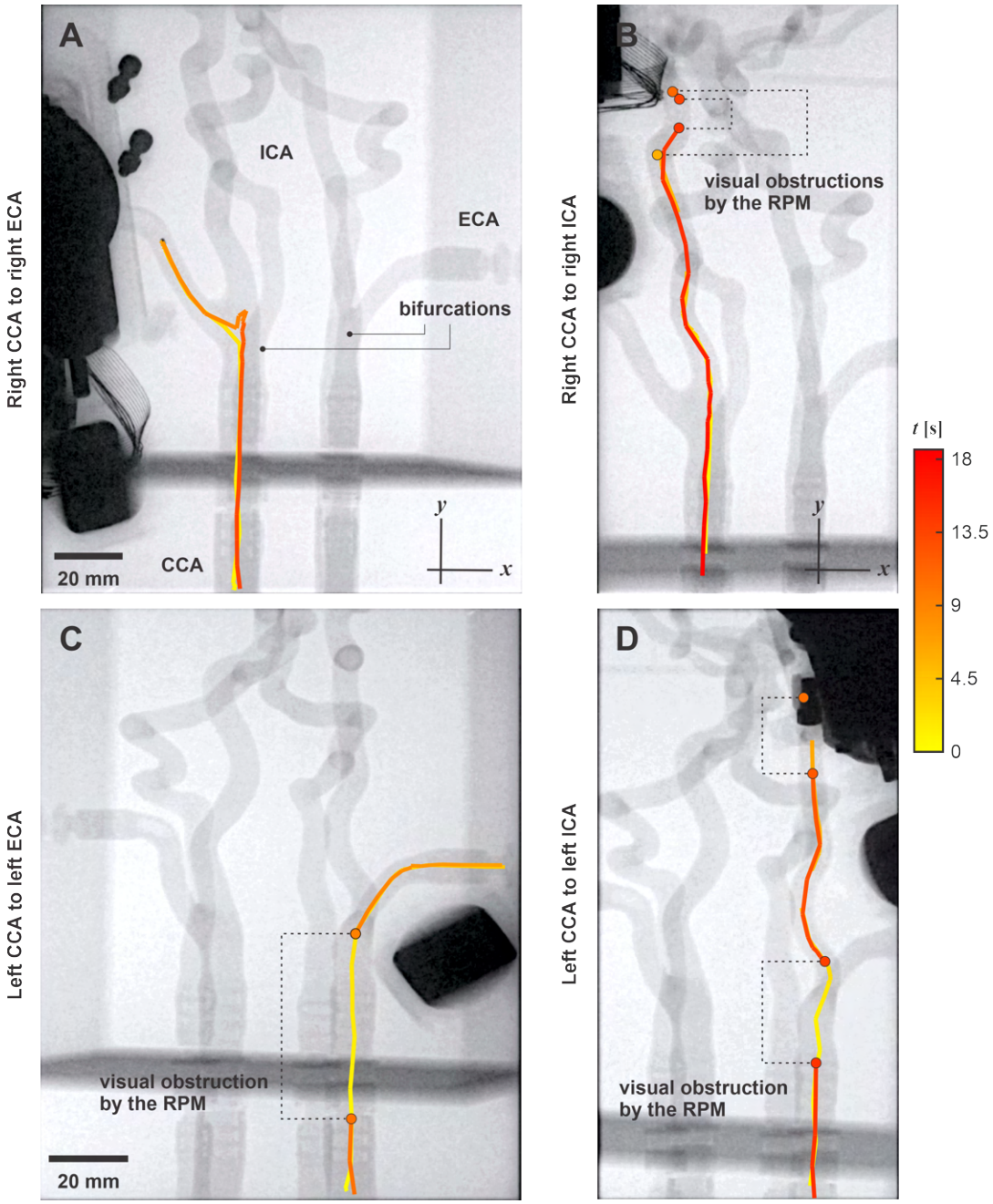

Fig. 4. The UMR is moved using X-ray-guided magnetic fields along desired paths within a cerebral vascular phantom. The black dashed lines indicate regions of visual obstruction in which the RPM obstructs the field of view between the detector and emitter of the C-arm. (A) The UMR is controlled to swim from the right common carotid artery (CCA) to the right external carotid artery (ECA). (B) Motion control is achieved between the right CCA to the right internal carotid artery (ICA). (C) The UMR is controlled between the left CCA to the left ECA. (D) Motion control is achieved between the left CCA to the left ICA. The location of the arteries (left and right) is defined in relation to the phantom. Please refer to supplementary multimedia.

adjusting the RPM-UMR gap based on Equation (1) to provide active suspension during helical propulsion [13]. The speed of the RPM has a linear relationship with the UMR speed at the desired actuation frequency and the distance covered, to ensure active suspension.

C. Description of Cerebral Vascular Phantoms

The cerebral vascular phantoms in this study replicate the intricate geometry of human cerebral vasculature, including arteries such as the internal carotid artery (ICA) with a diameter ranging from 4.3 to 5.8 mm, common carotid artery (CCA) with a diameter ranging from 7.7 to 8.2 mm, external carotid artery (ECA) with a diameter ranging from 4 to 4.3 mm, vertebral artery with a diameter ranging from 2 to 4 mm, posterior cerebral artery (PCA) with a diameter ranging from 2 to 3 mm, anterior cerebral artery (ACA) with a diameter of 2.8 mm, and middle cerebral artery (MCA) with a diameter ranging from 3 to 5 mm. They encompass diverse anatomical

TABLE I

THE UMR IS CONTROLLED TO SWIM ALONG THE LEFT AND RIGHT COMMON CAROTID ARTERY (CCA) TOWARD THE LEFT AND RIGHT EXTERNAL CAROTID ARTERY (ECA) AND INTERNAL CAROTID ARTERY (ICA). THE AVERAGE PATH VELOCITY (VAP) IS USED TO CHARACTERIZE THE MOTION ALONG EACH VASCULAR ROUTE. THE AVERAGE OBSTRUCTION TIME OVER THE INPUTTED PATH (AOTIP) IS USED TO CHARACTERIZE THE TIME WHEN NO POSITION COULD BE DETERMINED DUE TO OBSTRUCTION OF THE RPM. THE AVERAGES AND STANDARD DEVIATIONS ARE CALCULATED BASED ON 10 TRIALS ALONG EACH ROUTE FOR BOTH FORWARD AND BACKWARD VAP.

Vascular route	Route length [mm]	Forward VAP [mm/s]	Backward VAP [mm/s]	Total AOTIP [s]	Success rate [%]
Right CCA to right ECA	52.0	18.2 ± 6.1	10.8 ± 3.1	0.0 ± 0.1	83.3 ($n = 12$)
Right CCA to right ICA	134.1	14.5 ± 0.3	31.7 ± 1.2	2.0 ± 0.5	100 ($n = 10$)
Left CCA to left ECA	36.8	19.6 ± 2.1	14.0 ± 2.4	0.3 ± 0.3	83.3 ($n = 12$)
Left CCA to left ICA	127.4	19.3 ± 3.4	28.7 ± 3.4	3.0 ± 1.2	90.9 ($n = 11$)

features, including varying lengths and branching patterns, mimicking the complex anatomy of cerebral arteries, such as bifurcations, tortuous pathways, and variations in vessel diameter. Based on the varying diameters of the vascular routes, a UMR with a diameter of less than 2 mm should be able to navigate throughout the entire system. However, our 4-mm-diameter UMR is limited to navigating through the CCA toward either the ECA or the ICA due to its size.

III. EVALUATION OF WIRELESS CONTROL PERFORMANCE

A. Frequency Response Characterization

The frequency response of the UMRs is characterized within a range of 1 to 40 Hz, as depicted in Fig. 3(B). This range is constrained by the frequency capabilities of the RPM-actuator. The translational speed of the RPM shows a linear rise with the actuation frequency until 40 Hz, suggesting that the step-out frequency of the UMR exceeds 40 Hz. At each actuation frequency, the UMR is allowed to achieve straight runs along a transparent tube with a diameter of 9.525 mm and a UMR-RPM gap of 15 cm. This gap is clinically relevant and does not result in direct attraction of the UMR towards the RPM. The average speed is calculated offline from the captured camera footage, the shaded region represents the standard deviation. The determination of the drag coefficient c_{d} was conducted using COMSOL (COMSOL inc., Sweden), whereby the CAD model of the UMR was subjected to varying flow rates against its long axis. This analysis yielded an average c_{d} value of 0.94.

B. Motion Control inside the Cerebral Vascular Phantom

To showcase the controllable movement of the UMR within the cerebral vascular phantom, we establish four specific vascular routes. For each route, we conduct motion control tests consisting of at least ten successful runs, encompassing both forward and backward swimming movements. Please refer to supplementary multimedia.

1) Right CCA - right ECA: In this vascular route, the UMR starts from the proximal end of the right CCA and progresses towards the distal end of the right ECA, as depicted in Fig. 4(A). The UMR proceeds toward the bifurcation, then turns towards the right ECA, ascending toward its distal end. At $t = 9$ s, the UMR's motion direction is reversed, enabling it to swim downward along the ECA, and subsequently, it swims horizontally past the bifurcation along the CCA. At an actuation frequency of 9 Hz, the average path velocities (VAPs) for forward and backward motion are measured as 18.2 ± 6.1 and 10.8 ± 3.1 mm/s ($n = 10$), respectively. During traversal along the right CCA-right ECA route, only one visual obstruction was observed in the collected X-ray Fluoroscopy images, which equals a total obstruction time of 0.2 s ($n = 10$). The success rate along this route is calculated as 83.3% ($n = 12$).

2) Right CCA - right ICA: To navigate from the right CCA and reach the distal end of the right ICA, the UMR must traverse past the bifurcation of the ECA and the ICA, ascending along the ICA toward its distal end during the forward run. Along this route, the diameter of the vessel decreases progressively from 8.2 mm to 4.3 mm as the UMR advances. Therefore, the average VAP is 14.5 ± 0.3 mm/s. When the motion is reversed to enable the UMR to swim back toward the proximal end of the CCA, the UMR descends along the ICA from the distal end toward the bifurcation and then swims toward the proximal end of the CCA, at an average VAP of 31.7 ± 1.2 mm/s. Unlike the right CCA - right ECA route, two obstructions caused by the RPM-actuator are encountered during both the forward and backward runs, as shown in Fig. 4(B). For the ten trials along this vascular route, the average obstruction time over the path is measured to be 2.0 ± 0.5 s. However, due to the downward drift (along the $-\boldsymbol{z}$-axis) by the UMR, its preferred path is the bottom most bifurcation (as indicated in Fig. 4(A)), this resulted in an increased success rate along this vascular route of 100% ($n = 10$).

3) Left CCA - Left ECA: Now, we shift our focus to the left CCA and ECA. Similar to the previous trials, the UMR begins its movement from the proximal end of the left CCA, progresses toward the bifurcation, and then swims downward along the narrower left ECA, as depicted in Fig. 4(C). Along this vascular route, the average forward and backward VAP are measured as 19.6 ± 2.0 mm/s and 14.0 ± 2.4 mm/s, respectively. The average visual obstruction time over the path for the runs is measured as 0.3 ± 0.3 s and the success rate decreases to 83.3% ($n = 12$) due to the decreasing diameter of the ECA, which limits the movement of the UMR.

4) Left CCA - left ICA: Finally, during the navigation of the left CCA - left ICA route, additional visual obstruc-

tions are encountered, particularly during the backward run. Fig. 4(D) illustrates the UMR's forward movement from the proximal end of the left CCA toward the distal end of the left ECA. In this forward run, the UMR ascends toward the region with a decreasing diameter at an average VAP of 19.3 ± 3.4 mm/s. Upon reversing its motion, a visual obstruction is encountered along the left ICA. Another obstruction occurs as the UMR passes the bifurcation and enters the left CCA. However, despite these consecutive visual obstacles, the UMR maintains synchronization with the RPM. The average forward and backward VAPs are measured as 19.3 ± 3.4 mm/s and 28.7 ± 3.3 mm/s, respectively, while the average obstruction time over the path is measured as 3.0 ± 1.2 s and the success rate is 90.9% ($n = 11$).

C. Interpretation of Experimental Findings and Challenges

The experimental results of this study showcase the potential of UMRs for controlled navigation within a cerebral vascular phantom. Through rigorous testing across defined vascular routes, the UMRs demonstrated promising capabilities in maneuvering through complex vascular structures, overcoming challenges such as varying diameters and visual obstructions. The success rates obtained in controlling the UMRs through different vascular routes provide quantitative evidence of their effectiveness. The high success rates, ranging from 83.3% to 100% (Table I), underscore the reliability and precision of UMRs in navigating through cerebral vasculature. Notably, achieving a 100% success rate when navigating from the right CCA to the right ICA highlights the UMRs' adaptability to different vessel types and configurations.

However, it is worth noting the challenges encountered during the experiments, such as visual obstructions and varying diameters along the vascular routes. These challenges reflect real-world scenarios in neurosurgical procedures where precise navigation through tortuous and narrow vessels is crucial. Despite these challenges, the UMRs maintained stable control and successfully completed their designated paths, demonstrating robust performance under challenging conditions. While the 4-mm-diameter UMR successfully navigated from the CCA to either the ECA or the ICA, it was limited in its ability to access smaller cerebral arteries. The finding underscores the importance of UMR size optimization, suggesting that a smaller diameter, ideally below 2 mm, would enable comprehensive navigation throughout the entire vascular system of the phantom. This insight highlights a critical consideration for further development and refinement of UMR technology, emphasizing the need for size reduction to enhance versatility and applicability in neurosurgical interventions.

IV. CONCLUSIONS

This study confirms the viability of using UMRs for precise navigation within a cerebral vascular phantom. Through structured vascular routes and motion control trials, we demonstrate the UMRs' adeptness in navigating intricate vascular structures, addressing challenges such as varying diameters and visual obstructions. The success rates, ranging from 83.3% to 100% across different routes (i.e., left or right CCA toward left and right ECA or ICA), highlight the potential of UMRs for minimally invasive biomedical interventions in cerebral vasculature, offering promising advancements in neurosurgical procedures and the treatment of cerebrovascular conditions.

In future work, we plan to utilize an *ex vivo* model to simulate more realistic physiological conditions and anatomical complexities [14]. This will involve decreasing the size of the UMR to enable navigation throughout the entire vascular system of the *ex vivo* model, addressing the need for miniaturization to accommodate the intricate anatomy of cerebral vasculature. By incorporating an *ex vivo* model, we aim to evaluate the performance of UMRs in a more lifelike environment, considering factors such as blood flow dynamics and tissue interactions. This approach will provide valuable insights into the behavior and efficacy of UMR-based interventions, advancing their development and translation for neurosurgical procedures and cerebrovascular therapies.

REFERENCES

[1] R. Dreyfus et al., "Dexterous helical magnetic robot for improved endovascular access," *Sci. Robot.*, vol. 9, no. eadh0298, 2024.

[2] J. B. Mathieu, G. Beaudoin, and S. Martel, "Method of propulsion of a ferromagnetic core in the cardiovascular system through magnetic gradients generated by an MRI System," *IEEE Trans. Biomed. Eng.*, vol. 53, pp. 2929-2935, 2006.

[3] Q. Wang, L. Yang, J. Yu, P. W. Y. Chiu, Y.-P. Zheng, and L. Zhang, "Real-Time magnetic navigation of a rotating colloidal microswarm under ultrasound guidance," *IEEE Trans. Biomed. Eng.*, vol. 67, no. 12, pp. 3519-3528, Dec. 2020.

[4] T. Wang, H. Ugurlu, Y. Yan, et al., "Adaptive wireless millirobotic locomotion into distal vasculature," *Nat. Commun.*, vol. 13, article 4465, 2022.

[5] X. Liu et al., "Magnetic soft microfiberbots for robotic embolization," *Sci. Robot.*, vol. 9, no. eadh2479, 2024.

[6] T. Wang, H. Ugurlu, Y. Yan, et al., "Adaptive wireless millirobotic locomotion into distal vasculature," *Nat. Commun.*, vol. 13, p. 4465, 2022.

[7] L. Yang, T. Zhang, R. Tan, X. Yang, D. Guo, Y. Feng, H. Ren, Y. Tang, W. Shang, Y. Shen, "Functionalized spiral-rolling millirobot for upstream swimming in blood vessel," *Adv. Sci.*, vol. 9, p. 2200342, 2022.

[8] D. Jin et al., "Swarming self-adhesive microgels enabled aneurysm on-demand embolization in physiological blood flow," *Sci. Adv.*, vol. 9, p. eadf9278, 2023.

[9] L.-J.W. Ligtenberg, N.C.A. Rabou, C. Goulas, et al. "Ex vivo validation of magnetically actuated intravascular untethered robots in a clinical setting," Commun. Eng. vol. 3, no. 68, 2024.

[10] A. Hong, A. J. Petruska, and B. J. Nelson, "Tracking a magnetically guided catheter with a single rotating C-Arm," in *Proc. IEEE Int. Conf. Robot. Autom.*, Seattle, WA, pp. 618-623, 2015.

[11] J. Leclerc, H. Zhao, D. Bao, and A. T. Becker, "In vitro design investigation of a rotating helical magnetic swimmer for combined 3-D navigation and blood clot removal," *IEEE Trans. Robot.*, vol. 36, no. 3, pp. 975-982, 2020.

[12] T. W. R. Fountain, Prem V. Kailat, and J. J. Abbott, "Wireless control of magnetic helical microrobots using a rotating-permanent-magnet manipulator," in *Proc. IEEE Int. Conf. Robot. Autom.*, 2011, pp. 576–581.

[13] L.-J. W. Ligtenberg, I. A. A. Ekkelkamp, F. R. Halfwerk, C. Goulas, J. Arens, M. Warlé and I. S. M. Khalil, "Helical propulsion in low-Re numbers with near-zero angle of attack," in *Proc. IEEE Int. Conf. Intelligent Robots and Systems.*, 2023, pp. 2647-2652.

[14] A. Servant, F. Qiu, M. Mazza, K. Kostarelos, and B. J. Nelson, "Controlled in vivo swimming of a swarm of bacteria-like microrobotic flagella," *Adv. Mat.*, vol. 27, no. 19, pp. 2981-2988, Apr. 2015.